Extended proper orthogonal decomposition of non-homogeneous thermal fields in a turbulent pipe flow

Antonio Antoranz [a,b], Andrea Ianiro [a,*], Oscar Flores [a], Manuel García-Villalba [a]

[a] *Aerospace Engineering Group, Universidad Carlos III de Madrid, Avenida de la Universidad 30, 28911 Leganés, Spain*
[b] *Industria de Turbo Propulsores S.A., 28108 Alcobendas, Spain*

A B S T R A C T

This manuscript analyzes the role of coherent structures in turbulent thermal transport in pipe flows. A Proper Orthogonal Decomposition (POD) analysis is performed on a direct numerical simulation dataset with non-homogeneous boundary conditions, heated on the upper side, representative of solar receivers (Antoranz et al., 2015, Int. J. Heat Fluid Flow, 55). Three flow conditions are analyzed: with friction Reynolds number equal to 180 and Prandtl number equal to 0.7 and 4 and with friction Reynolds number equal to 360 and Prandtl number equal to 0.7. Both POD and extended POD modes are presented and compared. This allows to visualize the main flow modes in terms of both turbulent kinetic energy and temperature fluctuations, analyzing their contribution to the turbulent transport of heat. The POD analysis shows that the temperature fluctuations are described by a more compact modal subspace than the turbulent kinetic energy. The effect of increasing the Reynolds number is to produce a thinner boundary layer, with a slightly less compact representation of both kinetic energy and temperature fluctuations. The increase of the Prandtl number, instead, results in a thinner thermal boundary layer with a greater scale separation between thermal fluctuations and kinetic energy. Temperature POD modes together with velocity extended POD modes are used to analyze and quantify the mode contribution to turbulent thermal transport. Results show that the correlation between velocity and temperature is such that it is possible to describe roughly 100% of the turbulent heat transport and temperature fluctuations with only 40% of the kinetic energy. For the cases with $Pr = 0.7$, the first extended POD mode is a large vertical jet flanked by a pair of counter-rotating vortices near the heated part of the pipe. This single structure accounts for up to 10% of the turbulent heat transport.

© 2017 Elsevier Ltd. All rights reserved.

1. Introduction

Amongst the category of wall-bounded turbulent flows, pipe flows represent a canonical case which has been widely studied and is still object of intense research (see e.g. the recent thematic issue on high Reynolds number wall turbulence [1]). In spite of its importance and its wide range of applications in heat exchanger devices, literature is mostly focused on average heat transfer performance, starting from straight tubes (presented in well assessed textbooks, see, e.g. [2]) to curved tubes object of more modern researches [3]. Recent advances in numerical and experimental techniques have allowed to estimate surface heat transfer in pipes, especially focusing at heat transfer uniformity (see e.g. [4]). Nevertheless very few studies focus on the temporal variation of turbulent heat transfer at the wall and on the dynamical mechanism of

turbulent heat transfer. Recent attempts have been performed experimentally in [5] thanks to the development of time-resolved heat transfer sensors [6,7]. Few studies are dealing with resolved numerical simulation of pipe flows heat transfer mostly due to the computational complexity associated with the cylindrical coordinate system and the corresponding numerical singularity along the symmetry line. Some examples of Direct Numerical Simulations (DNS) of turbulent pipes flows with homogeneous heating are available [8–12].

Such resolved simulations allowed for the availability of high resolutions statistics and for the development of relations between wall heat flux and flow eddies. When comparing pipe flows with boundary layers flows, Saha et al. [12] suggest that, since pipe flow forces the motions near the centerline to interact more vigorously, the wall heat flux promotes stronger temperature fluctuations.

DNS data allow for the availability of full thermo-fluid-dynamic instantaneous information and makes possible to understand the thermo-fluid mechanisms inside the pipe. This is especially

---

Nomenclature

A	pipe cross-plane area
a_n	n^{th} mode temporal coefficient
$\underline{\underline{C}}$	two-point correlation matrix
$\overline{c_p}$	specific heat
$\underline{\underline{dA}}$	matrix containing local area values
$\overline{g}$	arbitrary scalar function
$\underline{\underline{g}}$	snapshot matrix of an arbitrary fluctuating scalar function g
Gr	Grashof number
K	integral measure of the turbulent kinetic energy in the pipe cross-section
m	wavenumber of the velocity POD spatial mode
N	number of modes
N_p	number of points in the spatial discretization
N_t	number of realizations
Pr	Prandtl number
q_w''	wall heat flux
R	pipe radius
Re	Reynolds number
Re_τ	friction Reynolds number
(r,θ,z)	cylindrical coordinates
T	temperature fluctuation with respect to the bulk temperature
T_b	bulk temperature
t	time
$\underline{u} = (u_1, u_2, u_3)$	velocity vector
u_τ	friction velocity
v	velocity component in the vertical direction
$\underline{x}$	spatial coordinate vector
(x, y, z)	cartesian coordinates

Greek symbols

α	thermal diffusivity
Γ	integral measure of the turbulent heat flux
Θ	integral measure of the temperature variance
λ_n	eigenvalues of the two-point correlation matrix
v	kinematic viscosity
ρ	density
$\underline{\underline{\Sigma}}$	matrix containing the singular values of the snapshot matrix
σ_n	n^{th} singular value of the snapshot matrix
τ_w	wall shear stress
$\underline{\underline{\varphi}}$	matrix of spatial modes
$\overline{\overline{\varphi}}_n$	n^{th} spatial mode
$\underline{\underline{\psi}}$	matrix of temporal modes

Subscripts

b	referred to a bulk quantity
k	referred to turbulent kinetic energy
max	maximum value
N	number of modes used for low-order reconstruction
T	referred to temperature
u_i	referred to the ith velocity component

Superscripts

$'$	referred to the temporal fluctuating part of a physical quantity
T	referred to a matrix transpose

relevant when dealing with problems where efficient turbulent transport and mixing are needed. An example of such problems is the flow inside the receivers of concentrated solar power towers [13]. The solar receivers are formed by thin-walled metal tubes, on which heliostats located around the tower concentrate the solar radiation while the fluid flowing through the tubes (typically a molten nitrate salt) increases its temperature due to the heat flux received. The solar receivers are irradiated only on their outward facing side and the flow inside the tubes experiences highly non uniform heat fluxes. One of the technical problems faced by these devices is that the tubes often break out due to the generated thermal stresses [14]. Experimental data is scarce, therefore efforts have been concentrated on developing simple models or using commercial computational fluid dynamics simulations to predict the performance of the tubes [15]. The operation of the plant must ensure the receiver safe operation, limiting the temperature of the heat transfer fluid and the temperature gradients on the wall. The operating conditions should try to, on one hand, increase the efficiency of the receiver, increasing the heat absorbed by the molten salts while flowing through the tubes, and on the other hand, reduce the salt temperature on the wall, the thermal stresses of the tubes and the pressure drop through the receiver. The strategies to improve the operation of the plant can be performed by changing the incident heat on the tubes (by varying the aiming strategy of the heliostats) or modifying the flow configuration of the receiver (modifying the inlet/outlet tubes of the receiver) [16]. Such challenges require a greater understanding of the flow and temperature distributions than currently available.

Direct numerical simulations of fully-developed turbulent flow and heat transfer in pipes, in which the temperature is regarded as a passive scalar, have been instrumental in understanding the mechanism of turbulent transport in pipes with non-homogeneous thermal forcing. Antoranz et al. [17] performed DNS simulations of incompressible flow in pipes with sinusoidal heating on the upper part and adiabatic conditions in the lower part, considering constant fluid properties. The friction Reynolds number (based on the pipe radius) was equal to 180 and 360 and the Prandtl number was equal to 0.7 and 4. Their results have shown that most of the turbulent thermal fluctuations take place in the upper part of the pipe where the heat flux is maximum. Reynolds number was found to have a small impact on the wall temperature distribution, while the Prandtl number produces significant changes, being the circumferential variations of temperature more pronounced in the case at higher Prandtl number.

A common approach in turbulent flows consists in decomposing, through Proper Orthogonal Decomposition, the fluctuating turbulent fields in orthogonal modes, which are representative of the main coherent structures of the flow [18]. Coherent structures include motions on different scales, ranging from near wall streaks to large and very large scale motions, which in a pipe might extend up to 20 pipe radii in the streamwise direction. Especially these large scale motions are found to be responsible of up to 50% of turbulent Reynolds stresses [19] and are especially interesting for the development of simplified models and the development of control strategies [20].

The POD modes are obtained as a weighted average of the snapshots and are optimal in an energy sense. The most common choice in turbulent flow studies is to decompose the velocity field, thus identifying the set of modes which is optimum in terms of turbulent kinetic energy. This procedure is well assessed in pipe flows, e.g. [21–24]. It can be shown that, for a fully developed flow where the statistical quantities are homogeneous in the tangential direc-

tion, POD modes converge to Fourier modes (see, e.g. [21]). These structures correspond to roll-cell like structures [25] that line up to create very large scale motions.

When dealing with multiple physical quantities, such as in the present case velocity and temperature fields, it can be interesting to analyse the proper orthogonal modes connected with other quantities of interest than the velocity. The extended proper orthogonal decomposition (EPOD, [26]) is based on the use of the same temporal basis to find the modes of any data ensemble synchronized with the data ensemble used for the decomposition, in order to extract information on correlated events. EPOD has been previously used to correlate several processes with flow coherent structures, e.g. wall pressures [27] and flame dynamics [28]. The analysis of the heat flux obtained from the thermal field synchronized with the velocity field has been approached using methods other than EPOD. Kruse and Von Rohr [29], for example, studied the structure of turbulent heat flux over a heated wavy wall by means of only POD analysis over Particle Image Thermometry data. They found good correlation between the first POD modes of thermal fluctuations and the first modes of the velocity fluctuations, as they were both highly influenced by the wavy wall geometry. In the present work, the dataset of Antoranz et al. [17] is analysed with POD and EPOD aiming at a better understanding of the heat transfer problem.

The manuscript is organized as follows. The database is introduced in Section 2. This is followed in Section 3 by a brief summary of the POD and EPOD methodologies. Then, numerical details on the snapshots considered are discussed in Section 4. Finally, results are presented and discussed in Section 5, followed by conclusions in Section 6.

2. Numerical database

The datasets to be analysed in this paper were generated by direct numerical simulations of a fully-developed turbulent pipe flow, with circumferentially-varying heat flux boundary condition. For completeness, we provide here the most important details of the computations; further details can be found in [17].

The governing equations are the Navier–Stokes equations for an incompressible flow together with an advection–diffusion equation for the internal energy. All fluid properties are considered constant, including the density, ρ, kinematic viscosity, v, thermal diffusivity, α, and specific heat c_p. Internal energy (thus temperature, given constant c_p) is treated as a passive scalar, i.e. it is assumed that the ratio between the Grashof number and the square of the Reynolds number $Gr/Re^2 \ll 1$.

The boundary conditions at the pipe wall are no-slip for the velocity and a circumferentially-varying heat flux given by

$$q''_w(\theta) = q''_{w,max} \sin \theta, \quad 0 < \theta < \pi \tag{1}$$

$$q''_w(\theta) = 0, \quad \pi < \theta < 2\pi \tag{2}$$

The added heat leads to a net increase of the temperature along the axial direction, z, which allows the decomposition of the temperature field in $T_b(z) + T(r, \theta, z, t)$, where r is the pipe radial coordinate, t is the time, $T_b(z)$ is the bulk temperature (averaged in time and in cross-planes) and T is the fluctuation with respect to the bulk temperature. Note that for a fully developed pipe flow, T is homogeneous along the axial direction and the time-averaged integral of T in cross-planes is zero.

Finally, the flow is driven by a constant pressure gradient in the axial direction. Hence, the velocity and the pressure gradient are homogeneous in the axial and circumferential directions. The temperature fluctuation is only homogeneous in the axial direction.

We analyze the three cases reported by Antoranz et al. [17]. These cases are defined by the values of the friction Reynolds num-

ber $Re_\tau = u_\tau R/v$ (where $u_\tau = \sqrt{\tau_w/\rho}$ is the friction velocity based on the wall shear stress τ_w) and the Prandtl number $Pr = v/\alpha$. Case 1 has $Re_\tau = 180$ and $Pr = 0.7$; case 2 has $Re_\tau = 180$ and $Pr = 4$; and case 3 has $Re_\tau = 360$ and $Pr = 0.7$.

All cases were simulated with Nek5000, a DNS spectral-element code developed by Fischer et al. [30]. The computational domain includes the full pipe volume over a length of $25R$, where R is the pipe radius. This domain is assumed to be periodic in the axial direction, due to the homogeneity of the velocity and temperature fluctuation fields in z. The computational domain is discretized with 55,440 spectral elements of polynomial order 7, with 105 elements in the stream-wise direction and 528 elements in the cross-planes. At the lower values of Re, the grid spacing is smaller than 3.5 wall units in the cross-plane and smaller than 9 wall units in the stream-wise direction. The outer grid point in the radial direction is located at 0.25 wall units from the wall.

3. Proper orthogonal decomposition of velocity and temperature fields

3.1. Fundamentals of proper orthogonal decomposition

In this section, a short introduction to Proper Orthogonal decomposition is presented. A complete discussion can be found in the book by Holmes et al. [18].

Consider $g(\underline{x}, t)$, a generic scalar function of the spatial coordinate $\underline{x}$ and time t. Using the Reynolds decomposition, $g(\underline{x}, t)$ can be expressed as the sum of a mean and a fluctuating field,

$$g(\underline{x}, t) = \langle g \rangle(\underline{x}) + g'(\underline{x}, t) = \langle g \rangle(\underline{x}) + \sum_{n=1}^{\infty} a_n(t)\varphi_n(\underline{x}) \approx$$
$$\approx \langle g \rangle(\underline{x}) + \sum_{n=1}^{N} a_n(t)\varphi_n(\underline{x}), \tag{3}$$

where $\langle g \rangle(\underline{x})$ and $g'(\underline{x}, t)$ indicate the mean and the fluctuating part of $g(\underline{x}, t)$. The mean value corresponds to the mathematical expectation. It coincides with the temporal mean of the samples acquired in an experiment or simulation if the process is ergodic; consequently it is possible to define:

$$\langle g \rangle(\underline{x}) = \lim_{N_t \to \infty} \frac{1}{N_t} \sum_{n=1}^{N_t} g(\underline{x}, t_n), \tag{4}$$
$$g'(\underline{x}, t) = g(\underline{x}, t) - \langle g \rangle(\underline{x}).$$

The fluctuating part can be approximated as a linear combination of a set of spatial basis functions $\varphi_n(\underline{x})$, with coefficients $a_n(t)$ depending on time; the symbol N is used to indicate the number of modes, i.e. the rank of the function space.

When choosing a basis function it is often advisable to make it orthonormal, i.e. that the inner product

$$\left(\varphi_n(\underline{x}), \varphi_p(\underline{x})\right) = \delta_{np}, \tag{5}$$

with δ_{np} the Kronecker delta equal to 1 for $n = p$ and to 0 for $n \neq p$. In the present study the inner product is defined as

$$\left(\varphi_n(\underline{x}), \varphi_p(\underline{x})\right) = \frac{\int \varphi_n(\underline{x})\varphi_p(\underline{x})\mathrm{d}\underline{x}}{\int \mathrm{d}\underline{x}} = \delta_{np}. \tag{6}$$

Proper Orthogonal Decomposition (POD, [31]) is a well assessed tool to extract information on the coherent structures in turbulent flows because it looks at the spatial basis of orthogonal functions $\varphi_n(\underline{x})$ with the larger mean square projections $\lambda_n = \langle (g'(\underline{x}, t), a_n(t)\varphi_n(\underline{x})) \rangle = \langle a_n(t)a_n(t) \rangle$.

This leads to the computation of the solution of the integral eigenvalue problem known as Fredholm equation which has as

kernel the two-point correlation of g, of which λ_n are the eigenvalues. Considering a set of N_t realizations $g_i(\underline{x})$ of $g(\underline{x},t)$, the integral equation has a discrete set of solutions: N_t eigenvalues λ_n of the two-point correlation matrix and N_t basis functions $\varphi_n(\underline{x})$. If in every realization, g is discretely sampled in space, e.g. each realization consists of N_p values along the spatial coordinate $\underline{x}$, following the snapshot method [32], it can be treated as an N_p-dimensional vector. The data can be arranged in a $N_t \times N_p$ snapshot matrix:

$$\underline{\underline{g}} = \begin{bmatrix} g'(x_1,t_1) & \cdots & g'(x_{N_p},t_1) \\ \vdots & \ddots & \vdots \\ g'(x_1,t_{N_t}) & \cdots & g'(x_{N_p},t_{N_t}) \end{bmatrix}. \tag{7}$$

At this point, if the spatial sampling is uniform, the modes can be determined solving the eigenvalue problem of the two-point correlation matrix of g with dimensions $N_t \times N_t$, i.e. $\underline{\underline{C}} = \underline{\underline{g}} \cdot \underline{\underline{g}}^T$ (being $\underline{\underline{g}}^T$ the transpose of $\underline{\underline{g}}$). Solving the eigenvalue problem of $\underline{\underline{C}}$ returns the eigenvalues λ_n and the left and right eigenvector matrices. The left and right eigenvector matrices are respectively the matrix $\underline{\underline{\psi}}$ containing in its columns the temporal modes $\underline{a}_n/\sqrt{\lambda_n}$ (which are orthonormal vectors of length N_t) and its inverse (i.e. its transpose). Note that the columns of $\underline{\underline{\psi}}$ are an orthonormal basis of rank N_t and are the *temporal modes* of $\underline{\underline{g}}$. The orthonormal spatial modes $\varphi_n(\underline{x})$ can then easily be computed as $\underline{\underline{\Sigma}} \cdot \underline{\underline{\varphi}} = \underline{\underline{\psi}}^T \cdot \underline{\underline{g}}$ where $\underline{\underline{\Sigma}}$ is a square diagonal matrix having the square root of the eigenvalues λ_n on its diagonal elements. The rows of $\underline{\underline{\varphi}}$ are orthonormal vectors and are the *spatial modes* of $\underline{\underline{g}}$. The elements of $\underline{\underline{\Sigma}}$ are called singular values of $\underline{\underline{g}}$. Consequently it is possible to express $\underline{\underline{g}} = \underline{\underline{\psi}} \cdot \underline{\underline{\Sigma}} \cdot \underline{\underline{\varphi}}$, which is the matrix-form analogous to Eq. (3).

The computation of the two-point correlation matrix $\underline{\underline{C}}$ is complicated whenever the spatial sampling of g is not uniform. Each element i,j of the two-point correlation matrix of g has to be computed as the scalar product of two realizations $(g_i(\underline{x}), g_j(\underline{x}))$ which in every point has to be weighted by the corresponding flow area, in order to reflect the different weights attributed by the non-uniform spatial sampling. This means that $\underline{\underline{C}} = \left(A^{-1} \underline{\underline{dA}} \circ \underline{\underline{g}} \right) \cdot \underline{\underline{g}}^T$ in which A is the total area of the flow under analysis, $\underline{\underline{dA}}$ is the matrix containing the local values of area corresponding to each point of the sampling grid and ∘ stands for the entry-wise Hadamard product (i.e. the ij^{th} element of $\underline{\underline{dA}} \circ \underline{\underline{g}}$ is equal to $dA_{i,j}g'_{i,j}$).

3.2. Extracting POD modes when dealing with multiple quantities and the need for extended POD

Whenever analysing realizations involving two or more dimensionally homogeneous quantities, i.e. a three-dimensional velocity vector field with $\underline{u} = (u_1, u_2, u_3)$, it is possible to determine the POD modes for each velocity component separately (i.e., using the two-point temporal correlation matrix for each velocity component). It is also possible to obtain POD modes which are optimal in the sense of the turbulent kinetic energy, using the sum $\underline{\underline{C}}_k$ of the two-point temporal correlation matrices of the three velocity components [18]. The POD modes obtained in each of these cases will be different, since they are optimal in a different norm. In other words, at the heart of a POD analysis, we always find the norm that defines the eigenvalue problem to be solved, and the physical interpretation of the POD modes critically depends on this norm.

The choice of a physically meaningful norm is specially complicated when dealing with non-dimensionally-homogeneous data (e.g, a velocity vector field and a density field). It has been shown

that, after a proper normalization, it is possible to sum the correlation matrices of all the physical quantities. The eigenvalues, in this case will contain the variance of a composite mode including both velocity and further physical quantities (e.g. density) [33]. Bailon-Cuba et al. [34] applied POD analysis for a Rayleigh-Bénard convection with heated bottom wall and cooled top wall. They studied the dependence of the heat transfer on the cell aspect ratio. The contribution of the different POD modes to the turbulent heat flux was obtained by creating a combined velocity-temperature norm with common temporal modes. The spatial modes were then not optimum neither in terms of the turbulent kinetic energy nor in terms of the temperature fluctuation variance.

The Extended Proper Orthogonal Decomposition (EPOD, [26]), instead, is based on the use of the same temporal basis obtained solving the eigenvalue problem of the correlation matrix of a generic quantity $g(\underline{x},t)$ to find the modes of whatever data ensemble synchronized with $g(\underline{x},t)$. EPOD allows then to extract information on correlated events between the two quantities.

In this work, EPOD is used to analyze the correlation between velocity and temperature, which is responsible for the turbulent transport of internal energy. Temporal bases are obtained solving the eigenvalue problem of both the fluid temperature correlation matrix, $\underline{\underline{C}}_T$, and the sum of the correlation matrices of the velocity components, $\underline{\underline{C}}_k$ The two temporal bases that are obtained, $\underline{\underline{\psi}}_T$ and $\underline{\underline{\psi}}_k$, are optimal in the least square sense for what concerns temperature fluctuation variance and for the description of turbulent kinetic energy, respectively. Temperature and velocity modes are then obtained from both bases:

$$\underline{\underline{\Sigma}}_{u_i,k} \cdot \underline{\underline{\varphi}}_{u_i,k} \quad = \underline{\underline{\psi}}_k^T \cdot \underline{\underline{u_i}}, \tag{8}$$

$$\underline{\underline{\Sigma}}_{T,k} \cdot \underline{\underline{\varphi}}_{T,k} \quad = \underline{\underline{\psi}}_k^T \cdot \underline{\underline{T}}, \tag{9}$$

$$\underline{\underline{\Sigma}}_{u_i,T} \cdot \underline{\underline{\varphi}}_{u_i,T} \quad = \underline{\underline{\psi}}_T^T \cdot \underline{\underline{u_i}}, \tag{10}$$

$$\underline{\underline{\Sigma}}_{T,T} \cdot \underline{\underline{\varphi}}_{T,T} \quad = \underline{\underline{\psi}}_T^T \cdot \underline{\underline{T}}, \tag{11}$$

where Eqs. (8) and (11) correspond to the standard POD modes of velocity and temperature, and (9) and (10) are the EPOD modes. The nature of each mode is indicated with the double subscripts in the terms on the left hand side, which show first the variable that is decomposed, and second the variable that has been used to compute the temporal basis. For instance, $\varphi_{u_i,T}$ corresponds to the spatial modes of the fluctuating velocity component u'_i obtained projecting the velocity snapshot matrix ($\underline{u_i}$) on the temporal basis ($\underline{\underline{\psi}}_T$) that results from the temperature correlation matrix ($\underline{\underline{C}}_T$). It has to be remarked here that the EPOD modes $\varphi_{u_i,T}$ and their norms $\underline{\underline{\Sigma}}_{u_i,T}$ account only for the part the turbulent kinetic energy correlated with the corresponding temporal mode of the temperature signal and vice versa. It is thus possible to obtain different power spectral densities amongst EPOD modes based on turbulent kinetic energy and on temperature. It is also possible to identify the parts of the correlation matrix $\underline{\underline{C}}_k$ which are poorly correlated with the temperature fluctuations, and thus contribute to the heat transport in a minimal amount.

4. Dataset description

The snapshot method described in Section 3 to obtain the POD and EPOD modes is applied here to the three cases presented in Antoranz et al. [17] and described in Section 2, namely case 1 ($Re_\tau = 180, Pr = 0.7$), case 2 ($Re_\tau = 180, Pr = 4$) and case 3 ($Re_\tau = 360, Pr = 0.7$). For every case, a snapshot dataset is obtained starting from 90 3D fields separated in time by $1.25R/u_\tau$, more than an eddy turnover time. Given the bulk velocity in the pipe,

turbulent eddies are convected downstream a distance of about 19R between two consecutive fields. From each field, 50 cross-plane slices have been extracted, with a separation of 0.5R between each pair of slices. The *snapshots* ensembles to be analysed are obtained from the mentioned slices. The temporal and spatial separation between the slices is assumed to be large enough to build a statistically significant dataset. The final dataset composed by the considered slices includes $N_t = 4500$ snapshots and has a spatial resolution of 69 and 100 points in the radial and azimuthal directions respectively.

5. Results and discussion

In the following, both standard snapshot POD modes and extended POD modes are presented. For standard snapshot POD modes, the nth eigenvalue of the snapshot correlation matrix, normalized with respect to the sum of all the correlation matrix eigenvalues, is represented as σ_n^2. It represents the *energy* contribution of each POD mode to the total turbulent fluctuation of a given quantity (turbulent kinetic energy or temperature fluctuation variance). For what concerns the EPOD modes, their turbulent kinetic energy contribution is estimated from the sum of the square of the diagonal elements of the $\underline{\underline{\Sigma}}_{u_i,T}$ matrices and is normalized with respect to the sum of all the velocity correlation matrix eigenvalues. The contribution of EPOD modes to temperature fluctuations is instead expressed as the square of the diagonal elements of $\underline{\underline{\Sigma}}_{T,k}$ normalized with respect to the sum of the eigenvalues of the temperature correlation matrix.

5.1. POD modes

The spectral contribution of velocity and temperature modes, optimal in sense of turbulent kinetic energy and temperature fluctuation variance, respectively, is reported in Fig. 1. This figure shows that the spectral contribution of the velocity modes to the turbulent kinetic energy is rather flat with the first mode accounting for about 2% of the turbulent kinetic energy. This is in agreement with Hellström and Smits [21] who found a quantitatively similar result. The first modes are slightly more energetic for the two cases at lower Reynolds number as a result of the greater spectral richness experienced in higher Reynolds number flows. The spectral contribution of temperature POD modes is reported in Fig. 1(b). Compared to the velocity modes, the energy contribution of the temperature modes is steeper. As a consequence the cumulative sum of the contributions to the temperature fluctuations

grows quicker at the beginning but slower for higher modes than the cumulative contributions to the kinetic energy (see insets in Fig. 1). Both the Prandtl and Reynolds numbers enhance the energy spreading over the modes spectrum; in fact the first temperature mode accounts for more than 7% of the temperature variance for the case at $Re = 180$ and $Pr = 0.7$, about 6.5% for the case at $Re = 360$ and $Pr = 0.7$ and about 4.5% for the case at $Re = 180$ and $Pr = 4$. This results might be ascribed to the fact that both the increase of the Reynolds number and the increase of the Prandtl number cause the decrease of the thermal boundary layer thickness, as discussed below when comparing POD and EPOD modes.

As an illustration, the first four turbulent kinetic energy and temperature modes for case 3 are presented in Fig. 2. Being the flow field statistically-homogeneous in the azimuthal direction and being the internal energy treated as a passive scalar, the velocity modes, in agreement with the literature, correspond to typical Fourier modes in the azimuthal direction. The most energetic pair of modes has a wavenumber $m = 2$, whilst the second pair of modes corresponds to a wavenumber $m = 3$ (see Fig. 2). Hellström and Smits [21] found qualitatively similar results but in different order, POD modes 1 and 2 showed a Fourier mode with wavenumber $m = 3$ and modes 3 and 4, wavenumber $m = 2$. Note that some authors make use of the azimuthal periodicity to decompose the POD modes by construction [35,22,36]. When this is not done, as in the present case, it has been shown that mode mixing might occur [21]. A mild mode mixing is observed for example in the modes 1 and 4 shown in Fig. 2(a) and (d). We have not enforced azimuthal periodicity by construction since the temperature POD modes do not present azimuthal symmetry, due to the non-homogeneous heat input. Instead, the heat input is symmetric with respect to the line $x = 0$, and the resulting temperature modes are either symmetric or antisymmetric with respect to this axis.

The first temperature mode, Fig. 2(e), contains a large scale temperature fluctuation in the upper part of the pipe, reaching beyond the thermal boundary layer. This might be connected with large scale motions in the outer region of the pipe boundary layer, which are very energetic as shown by Guala et al. [19]. Indeed, the first few turbulent kinetic energy modes represent large scale motions (see, e.g., Fig. 2) while near wall motions are captured by higher order modes (see Fig. 3 of Ref. [21]).

While the first temperature mode is symmetric with respect to $x = 0$, the second mode (Fig. 2(f)) is anti-symmetric and it is also concentrated in the upper part of the pipe. Higher order modes are harmonics of these first two modes, in the azimuthal and radial directions. For instance, the third mode (Fig. 2(g)) is a radial har-
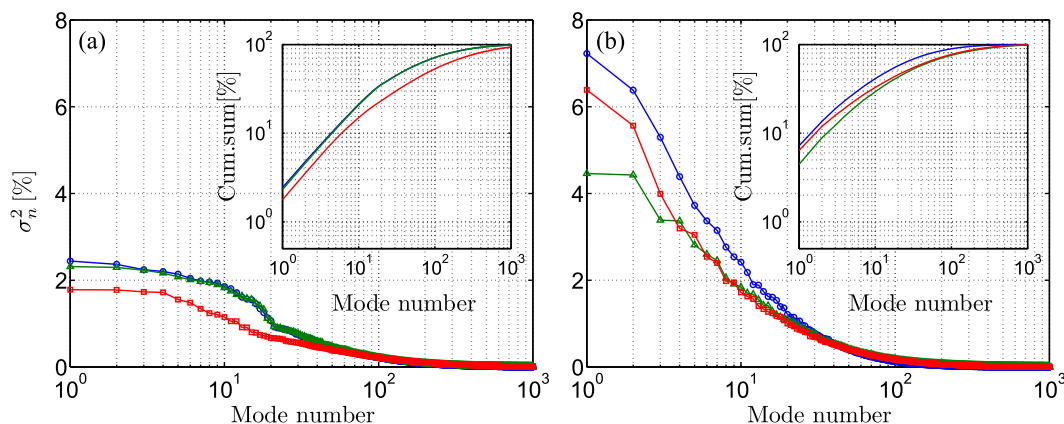

Fig. 1. Energetic contribution of the POD modes versus the mode number n. (a) Kinetic energy basis. (b) Temperature basis. The insets show the cumulative sum of the energetic contributions. Blue, case 1. Green, case 2. Red, case 3. (For interpretation of the references to color in this figure legend, the reader is referred to the web version of this article.)
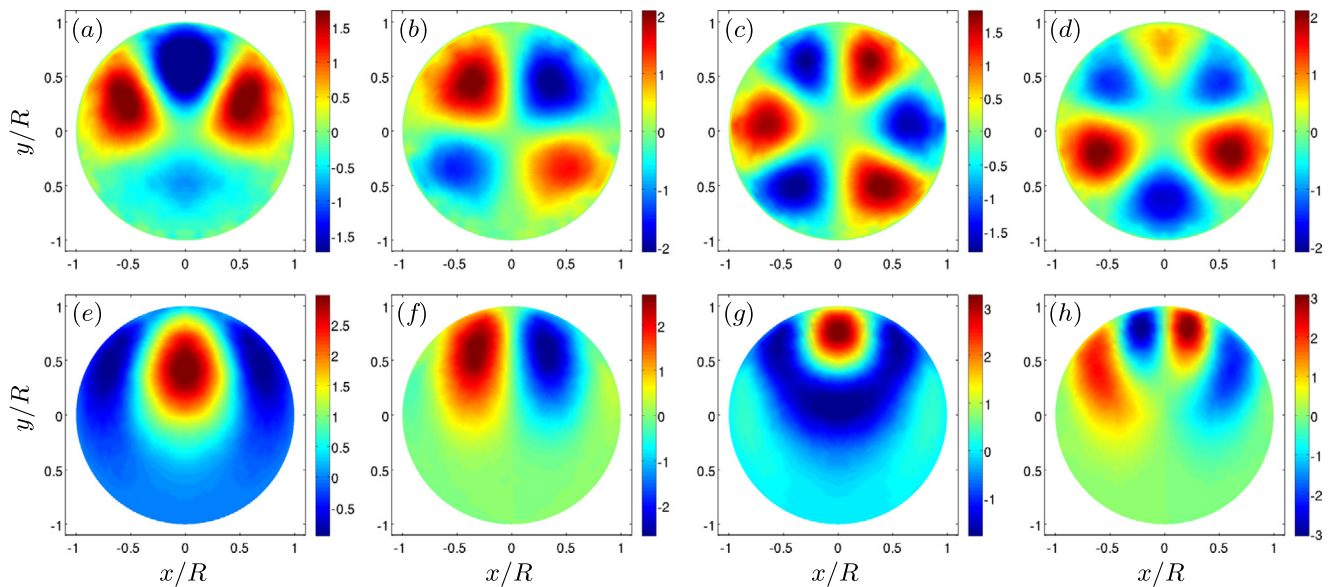
Fig. 2. First four POD modes of case 3. (a)–(d) Modes of the kinetic energy basis, color represents axial velocity fluctuations. (e)–(h) Modes of the temperature basis, color represents temperature fluctuations. (For interpretation of the references to color in this figure legend, the reader is referred to the web version of this article.)

monic of the first one, and the fourth mode (Fig. 2(h)) is an azimuthal harmonic of the second.

5.2. Extended POD modes

From the anaysis of the previous section, a main difference between the kinetic energy modes and the temperature modes is observed: while the former occupy the entire pipe section, the latter occupy mainly the upper part of the pipe, since the lower part of the pipe wall is adiabatic and temperature fluctuations are minimal in that region [17].

This is due to the fact that the thermal input is localized and does not influence the velocity field. Therefore, the use of EPOD to assess turbulent heat transport in this case is preferable. In other cases, where this distinction in not so clear, POD may suffice. We refer for example to the case of Kruse and Von Rohr [29] where both turbulence and thermal fluctuations where promoted by the presence of a wavy wall. In our case, the temperature can be considered a passive scalar, and it is therefore mainly governed by the convection from the flow field. Then, the EPOD modes of the velocity (Eq. (10)) show the part of the velocity fluctuation correlated to the temperature fluctuations. Note that the physical interpretation of temperature EPOD modes obtained from the temporal basis of the velocity POD modes (Eq. (9)) is less clear, due to the homogeneity in the azimuthal direction of the velocity POD modes.

Fig. 3 shows the energy contributions from both the POD and the EPOD modes for all three cases. Fig. 3(a)–(c) compare the energy contribution of the turbulent kinetic energy POD and EPOD modes (obtained from the temperature temporal basis). No significant differences are observed between the three cases considered. Overall, the EPOD mode contribution for the first few modes is roughly constant, and considerably smaller than the POD mode contribution (about one half). This is more evident from the observation of the cumulative sum in the corresponding inset that shows that with 1000 modes the POD mode contribution corresponds to about 99% while the EPOD mode contribution corresponds to roughly 40% of the total turbulent kinetic energy. This can be ascribed to the fact that the temperature temporal basis is biased towards events happening in the upper part of the pipe.

Note also that the contribution from the EPOD modes presents oscillations, indicating that the EPOD modes are not ordered.

Fig. 3(d)–(f) compare the energy contribution of the temperature POD and EPOD modes (obtained from the turbulent kinetic energy temporal basis). All the EPOD curves exhibit a fluctuating behaviour. However, the peaks for case 1 (Fig. 3(d)) and 3 (Fig. 3(f)) are more marked than for case 2 (Fig. 3(e)). For case 2, the energy contribution of any of the EPOD modes does not reach 2% and the higher energy content is reached in higher order modes such as mode 8 and 14. What is different in case 2 with respect to the other two cases is the Prandtl number ($Pr = 4$), which, being greater than one, results in a thermal boundary layer thinner than the momentum boundary layer. This favours the correlation between velocity and temperature for higher harmonics of the velocity (larger mode numbers). The EPOD mode contribution presents large spikes, since the modes are not ordered as discussed above. Finally, the large spikes appearing in the EPOD mode contributions of cases 1 and 3 are related to qualitative similitudes between POD modes of temperature and kinetic energy. For instance, in Fig. 3(f), the EPOD mode number 10 shows a peak of about 3% of the temperature variance. This is due to the fact that the mode 10 of the turbulent kinetic energy basis is qualitatively similar to the mode 1 of the temperature basis (here not shown for brevity).

Figs. 4–7 show, for the three cases, the first four POD modes of temperature together with the corresponding EPOD modes of velocity. Contours of the axial velocity are provided together with vectors illustrating the flow in the cross-plane. For cases 1 and 3, with the same Pr, the first four POD temperature modes are essentially equivalent, with mild differences. The shape of these modes was already discussed referring to Fig. 2(e)–(h). The difference between these two cases is the Re number, and this parameter does not seem to affect significantly the first few temperature modes. This reflects the fact that the more energetic modes in terms of temperature variance are related to large-scale flow structures, which are weakly dependent on the Reynolds number in the considered Reynolds number range. The first four POD temperature modes are significantly different for case 2, with $Pr = 4$, compared to cases 1 and 3, with $Pr = 0.7$. Thus, increasing Pr leads to POD temperature modes with fluctuations which occur closer to the
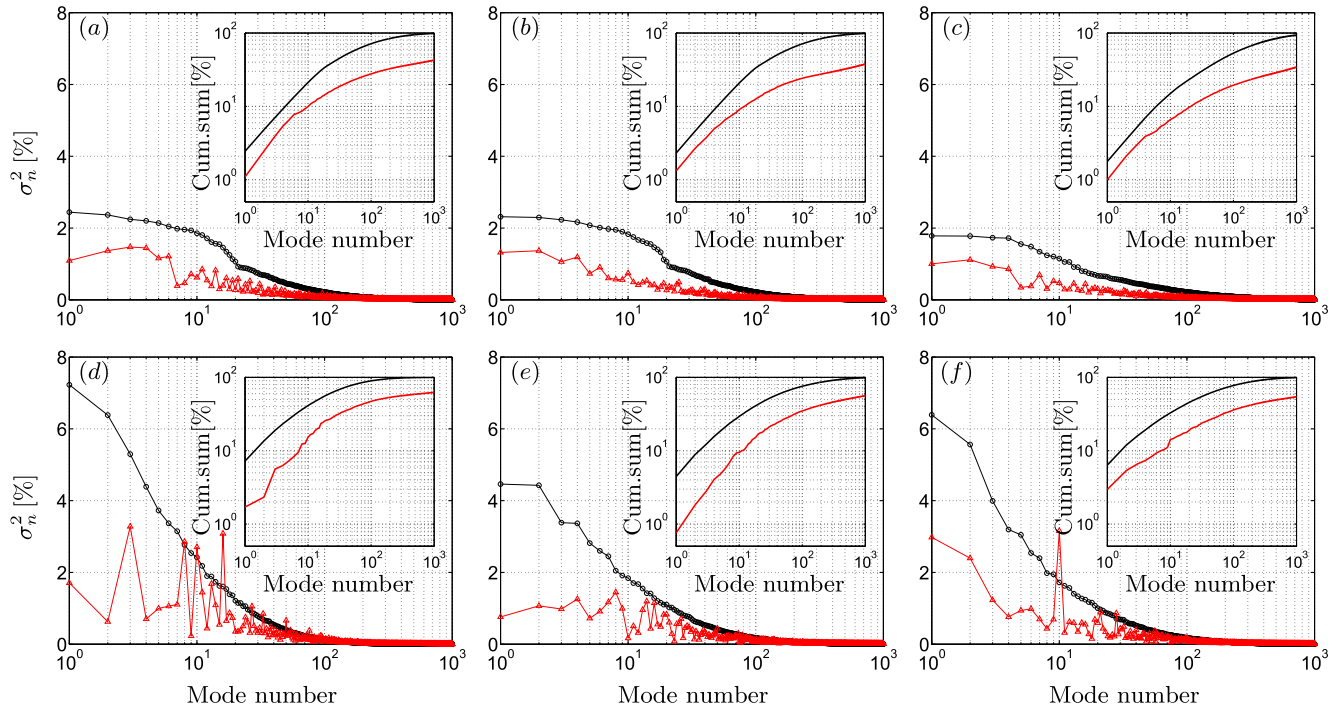
Fig. 3. Energetic contribution of the POD and EPOD modes versus the mode number n. (a), (d) Case 1. (b), (e) Case 2. (c), (f) Case 3. (a)–(c) Black line represents the contribution of the POD modes of the kinetic energy basis. Red line represents the kinetic energetic contribution of the EPOD modes of the temperature basis. (d)–(f) Black line represents the contribution of the POD modes of the temperature basis. Red line represents the temperature variance contribution of the EPOD modes of the kinetic energy basis. The insets show the cumulative sum of the corresponding energetic contributions. (For interpretation of the references to color in this figure legend, the reader is referred to the web version of this article.)
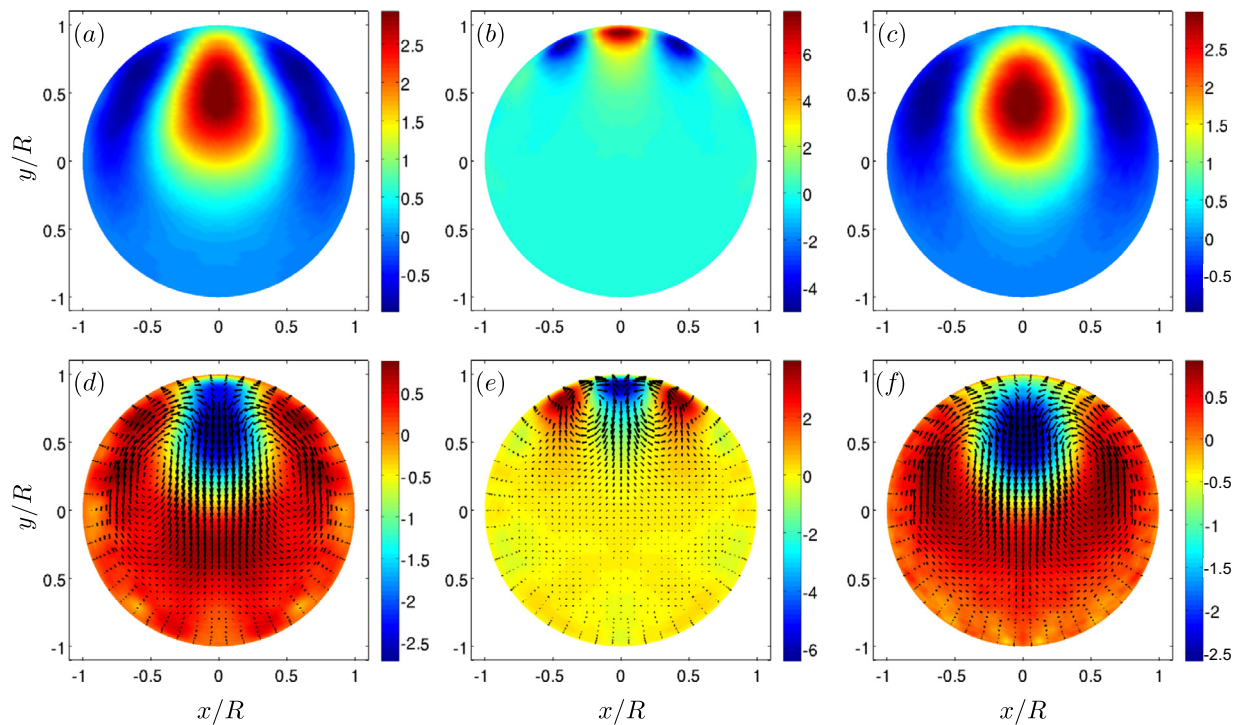

Fig. 4. POD and EPOD Mode 1. (a), (d) Case 1. (b), (e) Case 2. (c), (f) Case 3. (a)–(c) Temperature POD mode on temperature basis. (d)–(f) Velocity EPOD mode on temperature basis. Color represents axial velocity fluctuations, vectors represent cross-plane velocity fluctuations. (For interpretation of the references to color in this figure legend, the reader is referred to the web version of this article.)
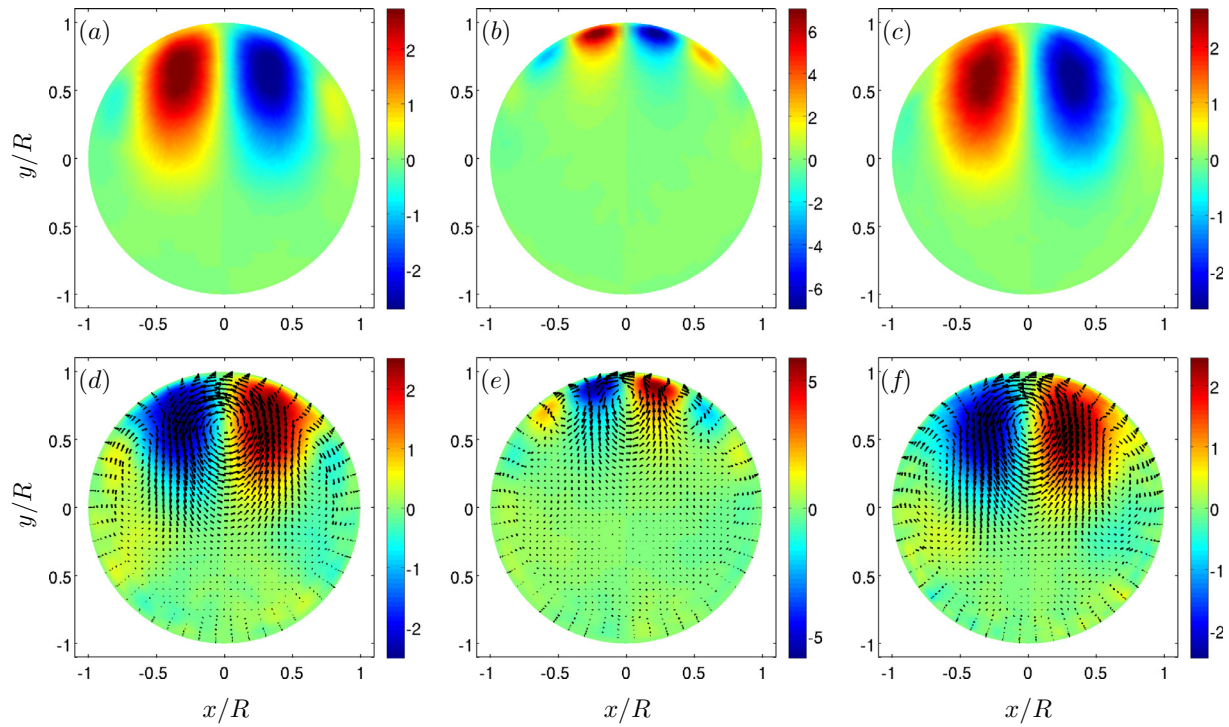
Fig. 5. POD and EPOD Mode 2. (a), (d) Case 1. (b), (e) Case 2. (c), (f) Case 3. (a)–(c) Temperature POD mode on temperature basis. (d)–(f) Velocity EPOD mode on temperature basis. Color represents axial velocity fluctuations, vectors represent cross-plane velocity fluctuations. (For interpretation of the references to color in this figure legend, the reader is referred to the web version of this article.)
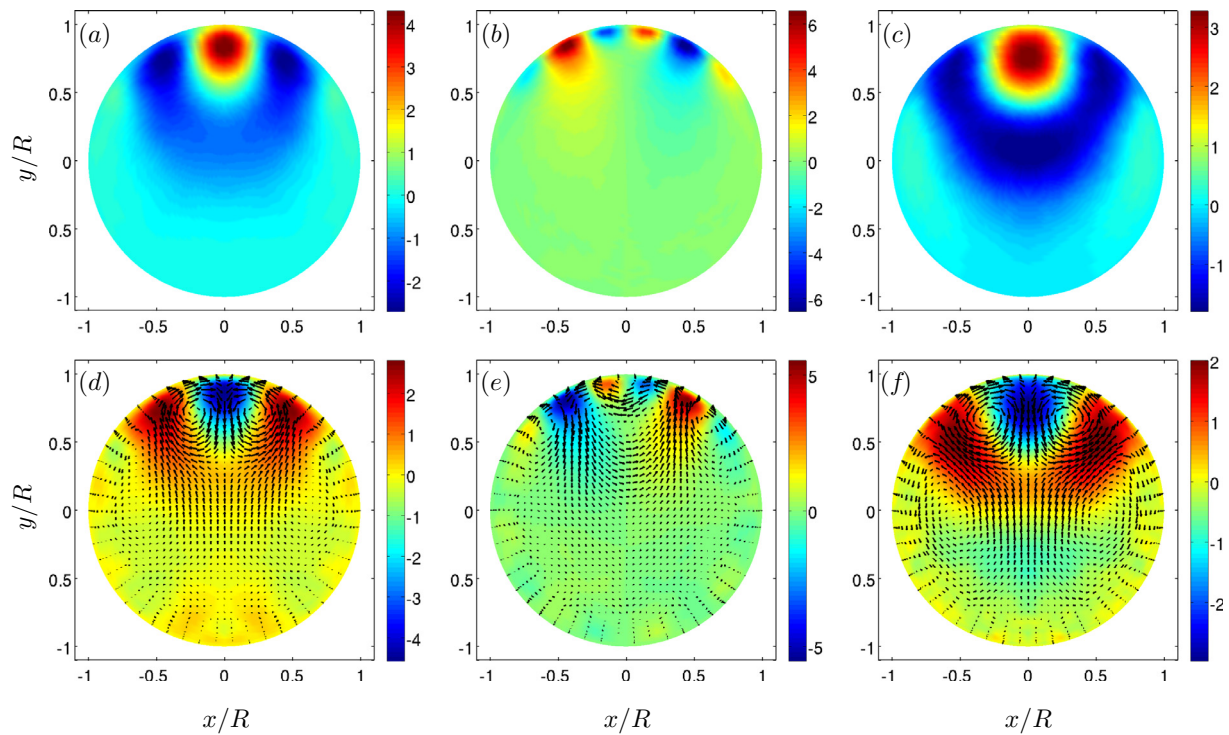

Fig. 6. POD and EPOD Mode 3. (a), (d) Case 1. (b), (e) Case 2. (c), (f) Case 3. (a)–(c) Temperature POD mode on temperature basis. (d)–(f) Velocity EPOD mode on temperature basis. Color represents axial velocity fluctuations, vectors represent cross-plane velocity fluctuations. (For interpretation of the references to color in this figure legend, the reader is referred to the web version of this article.)
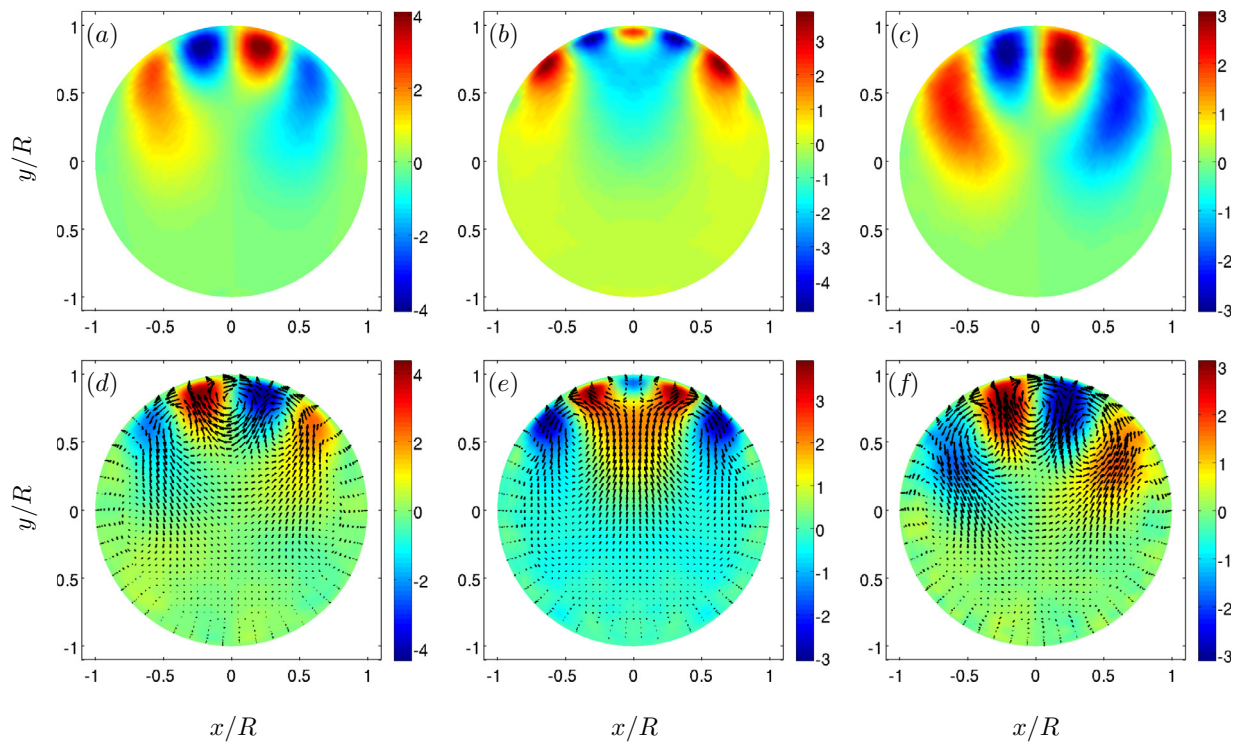
Fig. 7. POD and EPOD Mode 4. (a), (d) Case 1. (b), (e) Case 2. (c), (f) Case 3. (a)–(c) Temperature POD mode on temperature basis. (d)–(f) Velocity EPOD mode on temperature basis. Color represents axial velocity fluctuations, vectors represent cross-plane velocity fluctuations. (For interpretation of the references to color in this figure legend, the reader is referred to the web version of this article.)

top, Figs. 4(b)–7(b). Note that increasing *Pr*, the thermal boundary layer becomes significantly thinner than the momentum boundary layer and this phenomenon might be connected to this observation.

The difference between the POD modes of velocity and the EPOD modes of velocity estimated using the temperature basis is illustrated by comparing Fig. 2(a)–(d) to Figs. 4(f)–7(f). As already mentioned, while the POD modes occupy the whole pipe, the EPOD modes are concentrated in the upper part, where the convective heat transfer is taking place.

Figs. 4 and 5 also allow the combined analysis between a given temperature POD mode and its corresponding velocity EPOD mode, which is useful to identify the flow structures responsible of the convective heat transfer in the pipe. For example the first mode of case 1, Fig. 4(a), (d), is formed by a low speed region in the upper part of the pipe flanked by two counter-rotating vortices, driving a vertical jet in the central part of the pipe that transports downwards hot fluid, which returns near the (lateral) pipe walls. This is a symmetric mode with respect to the $x = 0$ plane. The second mode on the other hand is antisymmetric, Fig. 5(a), (d). It is formed by a high speed region and a low speed region side by side in the upper part of the pipe, with a vortex in between them. In the low (high) speed region, hot (cold) fluid is transported downwards (upwards) by the vortex. The remaining POD and EPOD modes shown in Figs. 4–7 can be analyzed in similar terms. A more quantitative analysis is provided in the following section.

5.3. Turbulent heat flux in the vertical direction

In the problem under consideration, heat is added to the system through the upper surface of the pipe, i.e. for $\theta \in (0, \pi)$, while the lower surface of the pipe, i.e. for $\theta \in (\pi, 2\pi)$, is adiabatic. The added heat is transported downwards, first by diffusive processes very near the wall and then by turbulent transport farther from the

wall. Then, heat is transported in the streamwise direction mainly by convection by the mean flow, leading to an increase of the bulk temperature along the pipe axis, as discussed in Section 2. The objective of this section is to analyze which flow structures contribute to the turbulent heat transport in the vertical direction (y), quantifying their contributions. This can be done using the POD-EPOD approach for analysing correlated events.

First, the turbulent heat flux in the vertical direction $\rho c_p \langle v'T' \rangle$ for the three cases is shown in Fig. 8(a)–(c), normalized with $q''_{w,max}$. Here, v' refers to the fluctuating velocity component in the vertical direction. As obtained from the DNS, the spatial distribution of the turbulent heat flux is similar for all cases. It is mainly negative, since the heat is transported downwards and decays to zero at the wall, since v' vanishes at the wall. For the three cases, the turbulent heat flux is concentrated in the upper part of the pipe, and the heat flux contours have a kidney shape. This might be due to the fact that the streamwise velocity is maximum at the core, leading to a stronger heat convection in the streamwise direction in this region, as compared to the mid-region of the pipe. Small differences can be observed between the three cases. For example, for case 1, Fig. 8(a), the region near the top where the turbulent heat flux is close to zero is somewhat thicker than in the other two cases. This is because the thermal boundary layer is thicker in case 1 than in case 2 (that has a larger *Pr*) and than in case 3 (that has a larger *Re*). This also results in somewhat larger values of the heat flux in cases 2 and 3, compared to case 1. Since the turbulent heat flux is concentrated in the upper part of the pipe, we have selected two heights for further analysis, namely $y_1 = 0.5R$ and $y_2 = 0.8R$, indicated by horizontal dashed lines in Fig. 8.

As mentioned in the previous section, the EPOD modes determine what velocity fluctuations are correlated to the temperature fluctuations. Therefore, we have reconstructed the temperature fields using the first N POD modes, $T'_N(\underline{x}, t)$, and the vertical velocity
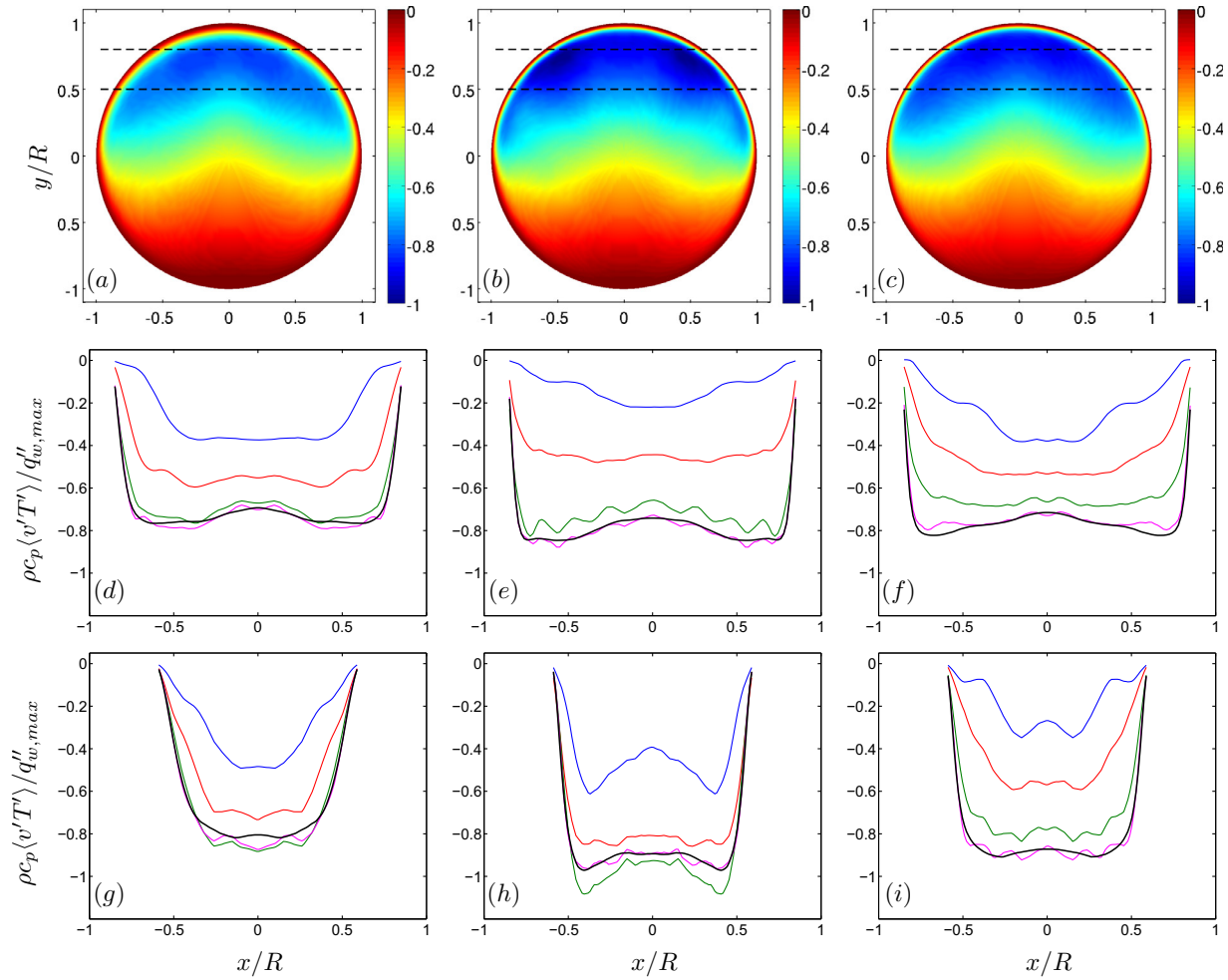
Fig. 8. (a)–(c) Turbulent heat flux in the vertical direction $\rho c_p \langle v'T' \rangle / q''_{w,max}$ obtained from the DNS. The dashed lines indicate the two heights at which the profiles are computed. (d)–(f) Profiles of the turbulent heat flux in the vertical direction at $y/R = 0.5$. (g)–(i) Profiles of the turbulent heat flux in the vertical direction at $y/R = 0.8$. DNS data (black). POD-EPOD reconstruction of the heat flux using 4 modes (blue), 16 modes (red), 64 modes (green) and 256 modes (magenta). (a), (d), (g) Case 1. (b), (e), (h) Case 2. (c), (f), (i) Case 3. (For interpretation of the references to color in this figure legend, the reader is referred to the web version of this article.)

fields using the corresponding N EPOD modes, $v'_N(\underline{x}, t)$. Using these fields, we compute a reconstructed turbulent heat flux $\rho c_p \langle v'_N T'_N \rangle$. Since in the present study, ρc_p is constant, in the following discussion we concentrate on the term $\langle v'T' \rangle$, disregarding ρc_p.

Fig. 8(d)–(f) shows the profile of $\langle v'T' \rangle$ at $y_1 = 0.5R$ for the three cases, together with the profiles of $\langle v'_N T'_N \rangle$ for $N = 4$, 16, 64 and 256. Fig. 8(g)–(i) shows the corresponding profiles at $y_2 = 0.8R$. At both heights, already with 16 modes we recover at least half of the heat flux while with 256 modes the reconstruction has already converged for the profiles shown, namely $\langle v'_{256} T'_{256} \rangle \approx \langle v'T' \rangle$. For case 1, at both heights, with 64 modes the reconstruction is very good, while for cases 2 and 3 with 64 modes the reconstruction can still be improved. Note that the contribution to $\langle v'_N T'_N \rangle$ of an individual pair of a temperature POD mode and a velocity EPOD mode can be either positive or negative. Hence, increasing the value of N, it is possible to overpredict the value of the heat flux, as for example in case 2 at $y_2 = 0.8R$ with 64 modes, Fig. 8(h). This means that there are some modes beyond $N = 64$ that represent an upward heat flux, so that in Fig. 8(h), the $N = 256$ reconstruction has converged to the actual value, as mentioned before.

In order to provide a more quantitative description of the heat flux reconstruction, we define an integral measure of the turbulent heat flux in the pipe. This can be easily done since everywhere $\langle v'T' \rangle \leq 0$, and the integral

$$\Gamma = \int_0^R \int_0^{2\pi} \langle v'T' \rangle r \mathrm{d}r \mathrm{d}\theta, \tag{12}$$

is a meaningful quantity. We define Γ_N as the corresponding integral computed using $\langle v'_N T'_N \rangle$. Fig. 9(a) shows for the three cases the ratio Γ_N / Γ (in %) as a function of the number of modes. This plot confirms that in case 1 ($Re_\tau = 180, Pr = 0.7$) less modes are required than in cases 2 ($Re_\tau = 180, Pr = 4$) and 3 ($Re_\tau = 360, Pr = 0.7$) to obtain a converged estimation of the turbulent heat flux in the whole domain, as already suggested by the profiles shown in Fig. 8. For $N < 10$, the contribution to the heat flux grows faster in case 3 than in case 2, however for $N > 10$ the trend reverses and it is the case 3 the one which requires more modes to obtain a converged estimation. For example, 94% of Γ is obtained with 256 modes in case 3. In cases 1 and 2 the percentage achieved with 256 modes is 99.3 % and 96.4%, respectively.

It is also meaningful to compare the reconstruction of the heat flux to the POD reconstruction of the temperature variance and the corresponding EPOD reconstruction of the turbulent kinetic energy. Therefore we define the integral measures of the temperature variance and the turbulent kinetic energy,

$$\Theta = \int_0^R \int_0^{2\pi} \langle T'T' \rangle r \mathrm{d}r \mathrm{d}\theta, \quad K = \frac{1}{2} \int_0^R \int_0^{2\pi} \langle u'_i u'_i \rangle r \mathrm{d}r \mathrm{d}\theta \tag{13}$$
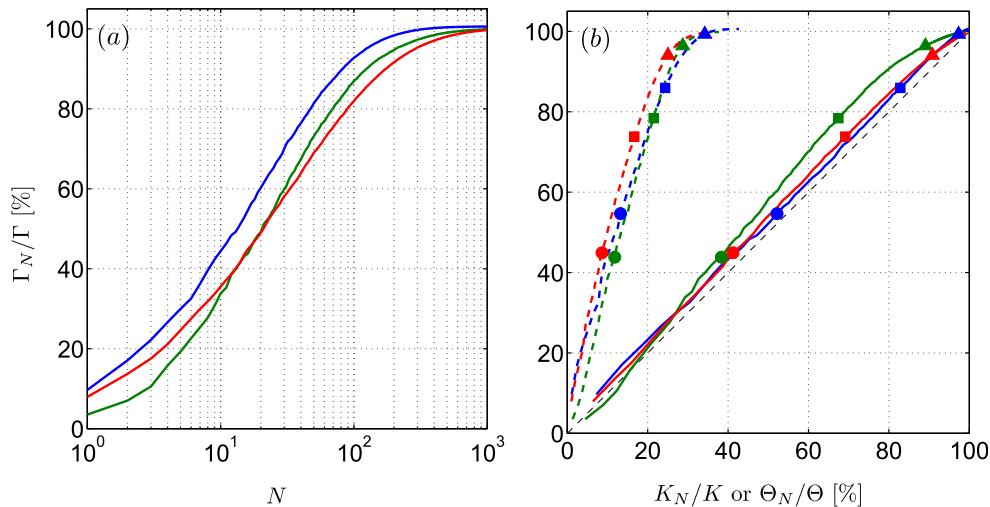
Fig. 9. Integral measure of the turbulent heat flux reconstruction Γ_N/Γ [%] vs. (a) Number of modes, (b) Integral measure of the kinetic energy reconstruction K_N/K [%] (dashed lines) and of the temperature variance reconstruction Θ_N/Θ [%] (solid lines). Blue, case 1. Green, case 2. Red, case 3. Circles, $N = 16$ modes. Squares, $N = 64$ modes. Triangles, $N = 256$ modes. The dashed black line in (b) is the line $y = x$ which is provided for reference. (For interpretation of the references to color in this figure legend, the reader is referred to the web version of this article.)

and the corresponding POD, Θ_N, and EPOD, K_N, reconstructions. Fig. 9(b) shows Γ_N/Γ as a function of K_N/K and as a function of Θ_N/Θ, for the three cases. It is remarkable that with 256 POD-EPOD modes more than 90% of the turbulent heat flux is recovered while the velocity fluctuations which are responsible for this turbulent transport only account to about 30% of the turbulent kinetic energy. This is explained by the fact that, although turbulent velocity fluctuations are present overall in the pipe, only those which reach the upper part of the pipe are effective in transporting heat. It is also noteworthy that the POD-EPOD reconstruction seems to be somewhat more efficient in estimating the turbulent heat flux than the POD reconstruction in estimating the temperature variance. This can be seen in Fig. 9(b), since for all three cases the line Γ_N/Γ vs. Θ_N/Θ is always slightly above the line $\Gamma_N/\Gamma = \Theta_N/\Theta$. This result is somewhat counterintuitive, since the POD modes are optimal in terms of the temperature variance. However, it is a consequence of the fact that the individual contributions of a POD/EPOD pair to Γ (or $\langle v'T' \rangle$) can be either positive or negative, while by definition the contribution of an individual temperature POD mode to Θ (or to $\langle T'T' \rangle$) is always positive. Then, moderately high-index POD/EPOD pairs that have zero net contributions to Γ still have (small) positive contributions to Θ.

6. Conclusions

In this paper we have analyzed a database of flow in a turbulent pipe with non-homogeneous thermal boundary conditions, with the main aim of identifying the motions responsible for the turbulent heat flux in the vertical direction. To this aim we have used a modal decomposition of instantaneous velocity and temperature fields in cross-planes. The modal decomposition employed is based on an extended proper orthogonal decomposition, in which the temperature is decomposed using standard proper orthogonal decomposition while the velocity is decomposed using the temperature temporal basis. This approach overcomes some of limitations of other heat transfer studies by means of modal decompositions [29,34]. Three flow conditions have been considered in order to assess the effect of both Reynolds and Prandtl numbers on the coherent motions responsible for the heat transport: friction Reynolds number equal to 180 and Prandtl number equal to 0.7 and 4 and friction Reynolds number equal to 360 and Prandtl number

equal to 0.7. Due to non-homogeneous heat flux boundary conditions, temperature and kinetic energy POD modes have a different spatial distribution, being the temperature fluctuations concentrated in the heated part of the pipe. The modal decomposition allows to discern which velocity fluctuations are correlated to the temperature fluctuations. Indeed we have shown that while standard POD modes of velocity are distributed over the whole pipe, extended POD modes of velocity are concentrated in the upper part of the pipe, where the vertical heat transfer is taking place. The combined analysis of a given POD temperature mode and its corresponding EPOD mode of velocity provides insights on the physical mechanisms of convective heat transfer. The study of the first few modes has resulted in the identification of the cross-plane vortices responsible for bringing hot fluid from the top to the pipe core. The size of these vortices seems to depend on the ratio between the thermal boundary layer thickness and the momentum boundary layer thickness, so that they are strongly affected by the Prandtl number.

Subsequently, we have reconstructed the temperature fields using POD modes and the vertical velocity fields using the corresponding EPOD modes. We have used these fields to compute a reconstructed turbulent heat flux in the vertical direction, finding that already with 16 modes we recover at least 50% of the total heat flux, while in all cases with 256 modes the reconstruction converges to the original heat flux. In addition, we have quantified the turbulent kinetic energy using the EPOD reconstructed velocity fields obtaining that with only 40% of the total turbulent kinetic energy we are able to reconstruct roughly 100% of the turbulent heat flux in the vertical direction. This result suggests that the present methodology is able to extract a relevant representation of the heat transport problem, which could have not been possible using a decomposition based on turbulent kinetic energy. The analysis presented in this article has shown that extended proper orthogonal decomposition appears to be a suitable tool to assess the flow features associated with temperature fluctuations, a tool that deserves to be embraced by the heat transfer community.

Conflict of interest

We have no conflict of interest to declare.

Acknowledgments

References

[1] J.C. Klewicki, G.P. Chini, J.F. Gibson, Prospectus: towards the development of high-fidelity models of wall turbulence at large Reynolds number, Phil. Trans. R. Soc. A 375 (2017) 20160092.

[2] F.P. Incropera, D.P. Dewitt, T.L. Bergman, A.S. Lavine, Fundamentals of Mass and Heat Transfer, John Wiley and Sons, 2002.

[3] P. Naphon, S. Wongwises, A review of flow and heat transfer characteristics in curved tubes, Renew. Sustainable Energy Rev. 10 (5) (2006) 463–490.

[4] L. Cattani, F. Bozzoli, S. Rainieri, Experimental study of the transitional flow regime in coiled tubes by the estimation of local convective heat transfer coefficient, Int. J. Heat Mass Tran. 112 (2017) 825–836.

[5] H. Nakamura, N. Shiibara, S. Yamada, Quantitative measurement of spatio-temporal heat transfer to a turbulent water pipe flow, Int. J. Heat Fluid Flow 63 (2017) 46–55.

[6] H. Nakamura, Frequency response and spatial resolution of a thin foil for heat transfer measurements using infrared thermography, Int. J. Heat Mass Tran. 52 (21) (2009) 5040–5045.

[7] M. Raiola, C.S. Greco, M. Contino, S. Discetti, A. Ianiro, Towards enabling time-resolved measurements of turbulent convective heat transfer maps with IR thermography and a heated thin foil, Int. J. Heat Mass Tran. 108 (2017) 199–209.

[8] M. Piller, Direct numerical simulation of turbulent forced convection in a pipe, Int. J. Numer. Methods Fluids 49 (6) (2005) 583–602.

[9] L. Redjem-Saad, M. Ould-Rouiss, G. Lauriat, Direct numerical simulation of turbulent heat transfer in pipe flows: Effect of Prandtl number, Int. J. Heat Fluid Flow 28 (5) (2007) 847–861.

[10] S. Saha, C. Chin, H.M. Blackburn, A.S.H. Ooi, The influence of pipe length on thermal statistics computed from DNS of turbulent heat transfer, Int. J. Heat Fluid Flow 32 (6) (2011) 1083–1097.

[11] E. Tavakoli, R. Hosseini, M. Papalexandris, B. Lessani, Statistical analysis of instantaneous turbulent heat transfer in circular pipe flows, Heat Mass Tran. 50 (1) (2014) 125–137.

[12] S. Saha, J.C. Klewicki, A.S.H. Ooi, H.M. Blackburn, Comparison of thermal scaling properties between turbulent pipe and channel flows via DNS, Int. J. Thermal Sci. 89 (2015) 43–57.

[13] R. Moore, M. Vernon, C.K. Ho, N.P. Siegel, G.J. Kolb, Design considerations for concentrating solar power tower systems employing molten salt, SAND2010-6978, Sandia National Laboratories, Albuquerque, NM, 2010.

[14] C. Marugán-Cruz, O. Flores, D. Santana, M. García-Villalba, Heat transfer and thermal stresses in a circular tube with a non-uniform heat flux, Int. J. Heat Mass Tran. 96 (2016) 256–266.

[15] M.R. Rodríguez-Sánchez, C. Marugán-Cruz, A. Acosta-Iborra, D. Santana, Comparison of simplified heat transfer models and CFD simulations for molten salt external receiver, Appl. Thermal Eng. 73 (1) (2014) 993–1005.

[16] M.R. Rodríguez-Sánchez, A. Sánchez-González, C. Marugán-Cruz, D. Santana, Flow patterns of external solar receivers, Sol. Energy 122 (2015) 940–953.

[17] A. Antoranz, A. Gonzalo, O. Flores, M. García-Villalba, Numerical simulation of heat transfer in a pipe with non-homogenous thermal boundary conditions, Int. J. Heat Fluid Flow 55 (2015) 45–51.

[18] P. Holmes, J.L. Lumley, G. Berkooz, C.W. Rowley, Turbulence, Coherent Structures, Dynamical Systems and Symmetry, second ed., Cambridge University Press, 2012.

[19] M. Guala, S.E. Hommema, R.J. Adrian, Large-scale and very-large-scale motions in turbulent pipe flow, J. Fluid Mech. 554 (2006) 521–542.

[20] C.W. Rowley, S.T.M. Dawson, Model reduction for flow analysis and control, Annu. Rev. Fluid Mech. 49 (2017) 387–417.

[21] L.H.O. Hellström, A.J. Smits, The energetic motions in turbulent pipe flow, Phys. Fluids 26 (12) (2014) 125102.

[22] L.H.O. Hellström, B. Ganapathisubramani, A.J. Smits, The evolution of large-scale motions in turbulent pipe flow, J. Fluid Mech. 779 (2015) 701–715.

[23] L.H.O. Hellström, I. Marusic, A.J. Smits, Self-similarity of the large-scale motions in turbulent pipe flow, J. Fluid Mech. 792 (2016), R1-1–R1-12.

[24] L.H.O. Hellström, A.J. Smits, Structure identification in pipe flow using proper orthogonal decomposition, Phil. Trans. R. Soc. A 375 (2017) 20160086.

[25] J.R. Baltzer, R.J. Adrian, X. Wu, Structural organization of large and very large scales in turbulent pipe flow simulation, J. Fluid Mech. 720 (2013) 236–279.

[26] J. Borée, Extended proper orthogonal decomposition: a tool to analyse correlated events in turbulent flows, Exp. Fluids 35 (2) (2003) 188–192.

[27] C. Picard, J. Delville, Pressure velocity coupling in a subsonic round jet, Int. J. Heat Fluid Flow 21 (3) (2000) 359–364.

[28] C. Duwig, P. Iudiciani, Extended proper orthogonal decomposition for analysis of unsteady flames, Flow Turbul. Combust. 84 (1) (2010) 25–47.

[29] N. Kruse, P.R. Von Rohr, Structure of turbulent heat flux in a flow over a heated wavy wall, Int. J. Heat Mass Tran. 49 (19) (2006) 3514–3529.

[30] P.F. Fischer, J.W. Lottes, S.G. Kerkemeier, nek5000 Web page, http://nek5000.mcs.anl.gov, 2008.

[31] G. Berkooz, P. Holmes, J.L. Lumley, The proper orthogonal decomposition in the analysis of turbulent flows, Annu. Rev. Fluid Mech. 25 (1993) 539–575.

[32] L. Sirovich, Turbulence and the dynamics of coherent structures. Part I: Coherent structures, Quart. Appl. Math. 45 (1987) 561–571.

[33] J.L. Lumley, A. Poje, Low-dimensional models for flows with density fluctuations, Phys. Fluids 9 (7) (1997) 2023–2031.

[34] J. Bailon-Cuba, M.S. Emran, J. Schumacher, Aspect ratio dependence of heat transfer and large-scale flow in turbulent convection, J. Fluid Mech. 655 (2010) 152–173.

[35] J.H. Citriniti, W.K. George, Reconstruction of the global velocity field in the axisymmetric mixing layer utilizing the proper orthogonal decomposition, J. Fluid Mech. 418 (2000) 137–166.

[36] A. Duggleby, K.S. Ball, M. Schwaenen, Structure and dynamics of low Reynolds number turbulent pipe flow, Phil. Trans. R. Soc. A 367 (1888) (2009) 473–488.